

Testing the blazar spectral sequence: X-ray-selected blazars

L. Maraschi,¹★ L. Foschini,² G. Ghisellini,¹ F. Tavecchio¹ and R. M. Sambruna³

¹INAF – Osservatorio Astronomico di Brera, V. Brera 28, I-20100 Milano, Italy

²INAF–IASF Bologna, Via Gobetti 101, 40129 Bologna, Italy

³NASA Goddard Space Flight Center, Code 661, Greenbelt, MD 20771, USA

Accepted 2008 October 1. Received 2008 October 1; in original form 2008 July 23

ABSTRACT

We present simultaneous optical and X-ray data from *Swift* for a sample of radio-loud flat-spectrum quasars selected from the Einstein Medium Sensitivity Survey (EMSS). We present also a complete analysis of *Swift* and *INTEGRAL* data on four blazars recently discussed as possibly challenging the trends of the hypothesized ‘blazar spectral sequence’. The spectral energy distributions (SEDs) of all these objects are modelled in terms of a general theoretical scheme, applicable to all blazars, leading to an estimate of the jets’ physical parameters. Our results show that, in the case of the EMSS broad line blazars, X-ray selection does not lead to find sources with synchrotron peaks in the UV/X-ray range, as was the case for X-ray-selected BL Lacs. Instead, for a wide range of radio powers all the sources with broad emission lines show similar SEDs, with synchrotron components peaking below the optical/UV range. The SED models suggest that the associated inverse Compton (IC) emission should peak below the GeV range, but could be detectable in some cases by the Fermi Gamma-ray Space Telescope. Of the remaining four ‘anomalous’ blazars, two highly luminous sources with broad lines, claimed to possibly emit synchrotron X-rays, are shown to be better described with IC models for their X-ray emission. For one source with weak emission lines (a BL Lac object) a synchrotron peak in the soft X-ray range is confirmed, while for the fourth source, exhibiting narrow emission lines typical of narrow-line Seyfert 1 galaxies, no evidence of X-ray emission from a relativistic jet is found. We re-examine the standing and interpretation of the original ‘blazar spectral sequence’ and suggest that the photon ambient, in which the particle acceleration and emission occur, is likely the main factor determining the shape of the blazar SED. A connection between SED shape and jet power/luminosity can however result through the link between the mass and accretion rate of the central black hole and the radiative efficiency of the resulting accretion flow, thus involving at least two parameters.

Key words: radiation mechanisms: non-thermal – galaxies: active – galaxies: jets.

1 INTRODUCTION

The spectral energy distributions (SED) of blazars from radio to γ -rays exhibit remarkable properties, in particular a ‘universal’ structure consisting of two broad humps. A systematic compilation of multiwavelength data for three complete samples, two selected in the radio band (2-Jy FSRQ and 1-Jy BL Lacs) and one in X-rays (Einstein Slew Survey BL Lacs) was performed by Fossati et al. (1998). Note that, at the time, the results from the Compton Gamma-ray Observatory (CGRO) were still under study, while very few objects had been detected in the TeV band, thus the data at high energies were rather incomplete.

The derived SEDs were averaged in fixed radio luminosity bins, *irrespective of sample membership or classification (BL Lac versus*

FSRQ). The result was the well-known ‘spectral sequence’ (a series of five average SEDs, ‘sequence’ in the following) showing the peaks of the two spectral components shifting systematically to higher frequencies with decreasing luminosity. For brevity we will refer to SEDs with synchrotron peak below or above the optical range as ‘red’ or ‘blue’ SEDs, respectively.

It has to be stressed that the derived average SEDs, by themselves, only represent the spectral properties of the considered samples and do not contain further implications; however the fact that, despite the mixing of different samples and classifications, the average SEDs show systematic trends, possibly driven by the radio power *suggests* an underlying regularity of behaviour of jets in very different objects. Understanding this behaviour could lead to a more profound comprehension of the jets’ radiation mechanisms and physics.

Ghisellini et al. (1998) modelled a large number of individual sources with sufficient data at high energies with a simple general scheme: a single emission region, moving with bulk Lorentz

★E-mail: laura.maraschi@brera.inaf.it

factor $\Gamma \simeq 10$, contains relativistic electrons emitting via synchrotron radiation the lower energy spectral component; the same electrons up scatter synchrotron photons as well as photons from an external radiation field producing the high-energy spectral component. The electron spectrum is computed assuming a broken power-law injection spectrum and taking into account radiative energy losses.

With these minimal assumptions the ‘sequence’ of spectral properties translates into a parameter sequence, in which the energy of the electrons radiating at the SED peaks is higher for lower values of the (comoving) total magnetic field plus photon energy densities, due to the reduced energy losses. This interpretation of the ‘sequence’ concept and following developments (Costamante & Ghisellini 2002; Ghisellini, Celotti & Costamante 2002) led to successful predictions of the best candidates for TeV detection (see Wagner 2008, for a recent review).

On the other hand, the phenomenological ‘sequence’ is likely affected by observational biases (Maraschi & Tavecchio 2001). Significant efforts were made to construct new samples of blazars with different thresholds and selection criteria (e.g. Laurent-Muehleisen et al. 1999; Caccianiga & Marchã 2004; Massaro et al. 2005; Landt, Perlman & Padovani 2006; Giommi et al. 2007a; Turriziani, Cavazzuti & Giommi 2007; Healey et al. 2008; Massaro et al. 2008) and some discrepant objects were found (see Padovani 2007 for a review on the challenges to the blazar sequence). In particular Caccianiga & Marchã (2004) evidenced the existence of sources with relatively low radio power, but X-ray to radio ratios similar to those of FSRQs.

In a somewhat different line of approach the group led by Valtaoja developed a technique to estimate the beaming parameters (Doppler factors Lorentz factors and viewing angles) of blazar jets from the radio properties alone (Valtaoja et al. 1999; Lähteenmäki & Valtaoja 1999; Lähteenmäki, Valtaoja & Wiik 1999). Basing on extensive monitoring data at high radio frequencies (22 and 37 GHz) these authors compute ‘apparent’ brightness temperatures using light traveltimes inferred from variability as sizes for the emission region. Comparing the results with the theoretical maximum brightness temperature allowed by the SSC process they derive the Doppler factor of the emission region and further use the apparent superluminal speeds to determine the bulk Lorentz factor and the viewing angle. This procedure is correct; however, one has to keep in mind that the results obtained refer to the radio-emitting regions of the jet, which do not coincide with the regions emitting the high-energy radiation (e.g. Ghisellini et al. 1998; Sikora 2001). Moreover, in the analysis of the SEDs of a large number of BL Lac objects Nieppola, Tornikoski & Valtaoja (2006) fit the data in the full (radio to γ -ray) frequency range available with a single parabolic curve, thus their determination of the ‘peak frequency’ of the SED cannot be compared with our approach. In Nieppola et al. (2008) however, the parabolic fits are not forced to include the X-ray and higher energy data, yielding peak frequencies that can be compared with ours. We will discuss their results in Section 6.

One of the problems in the ‘sequence’ assembly was the lack of an X-ray-selected sample of flat-spectrum radio quasars. Wolter & Celotti (2001) selected and discussed a sample of FSRQ within the X-ray-selected sample of radio-loud active galactic nuclei (AGN) from the Einstein Medium Sensitivity Survey (EMSS). They found that the average broad-band spectral indices of these X-ray-selected FSRQs were consistent with those of the radio-selected FSRQs within the ‘sequence’. However, a study of their SEDs was not possible due to insufficient spectral data.

Here, we present *Swift* observations of the 10 X-ray brightest objects in the Wolter & Celotti sample as well as a full analysis of *Swift* data for four blazars recently claimed to be at odds with the sequence scheme. We model the SEDs of the 14 objects following Ghisellini et al. (2002), deriving estimates of important physical quantities for their jets. Finally, in the light of these new results, we discuss the present standing and interpretation of the blazar ‘spectral sequence’. Preliminary results were given in Maraschi et al. (2008). The scheme of the paper is as follows. Section 2 gives information on the selected sources and Section 3 describes the data and analysis methods. Section 4 details the general spectral modelling procedure. The results are presented in Section 5. A general discussion is given in Section 6 while the conclusions are given in Section 7.

2 THE SOURCES

2.1 The X-ray-selected radio-loud AGN sample from the Einstein Medium Sensitivity Survey

Wolter & Celotti (2001) selected 39 radio-loud, broad line AGN from the X-ray EMSS sample (Gioia et al. 1990; Stocke et al. 1991). Of these, 20 had a measured radio spectral index $\alpha_r < 0.7$ and their broad-band properties were compared to those of classical radio-selected flat-spectrum quasars. Their broad-band indices (α_{ro}, α_{ox}) were found to be similar to those of FSRQ. This is at odds with the case of BL Lac objects, which occupy very different regions in the α_{ro}, α_{ox} plane depending on whether they derive from X-ray or radio selection. On the other hand, broad-band indices give only a global information, which may be ambiguous (see below). We therefore decided to exploit the unique capabilities of the *Swift* satellite to observe the ten X-ray brightest FSRQs of the EMSS sample in order to derive their X-ray spectrum together with simultaneous optical data allowing a reliable snapshot of the optical to X-ray SED. Observations were performed within the filler program. The data gathered and analysis methods are described in Section 3.

2.2 Controversial sources

In addition to the EMSS sources, we include in our analysis and discussion four sources of controversial classifications put forward by other authors: two ultraluminous, high-redshift, broad line quasars recently discovered, SDSS J081009.94+384757.0 ($z = 3.946$, Giommi et al. 2007b) and MG3 J225155+2217 ($z = 3.668$, Bassani et al. 2007) have been claimed, on the basis of their broad-band spectral indices, to show a *synchrotron* peak in hard X-rays. If confirmed, these claims would imply strong violations of the sequence scheme.

Two other cases concern blazars of intermediate luminosities, namely RX J1456.0+5048 ($z = 0.478$; Giommi 2008) and RGB J1629+401 ($z = 0.272$; Padovani et al. 2002), which show synchrotron peaks in the X-ray band and, in addition, exhibit emission lines, weak in the first source and pronounced, but narrow, in the second one. For these four objects, all the existing data obtained with *Swift* and, in the case of MG3 J225155+2217 also the data obtained with *INTEGRAL* were systematically reanalysed to produce a data set as homogeneous and complete as possible.

3 DATA ANALYSIS

All the data presented here were analysed in the same way to guarantee a homogeneous treatment. The common procedures adopted for the analysis are described below.

3.1 *Swift*

The data from all three instruments onboard *Swift*, namely BAT, XRT and UVOT (Gehrels et al. 2004), have been processed and analysed with HEASOFT v. 6.3.2 with the CALDB released on 2007 November 11. The observation log is reported in Table 1.

The X-ray telescope (XRT; 0.2–10 keV; Burrows et al. 2005) data were analysed using the xrtpipeline task, selecting single to quadruple pixel events (grades 0–12) in the photon-counting mode.

Table 1. *Swift* observation log.

Source	ObsID	Date
MS 0152.4+0424	00036502001	28-06-2007
	00036502002	11-01-2008
MS 0232.5–0414	00036503001	21-02-2008
	00036503002	22-02-2008
MS 0402.0–3613	00035523001	24-03-2006
	00035523002	29-03-2006
	00036504001	27-07-2007
	00036504002	08-08-2007
MS 0521.7+7918	00036504003	30-12-2007
	00036504004	01-01-2008
	00036505001	01-12-2007
	00036505002	02-12-2007
MS 0828.7+6601	00036505003	04-12-2007
	00036506001	23-01-2008
MS 1050.9+5418	00036507001	24-01-2008
	00036507002	27-01-2008
MS 1234.9+6651	00036508001	18-05-2007
	00036508002	12-07-2007
	00036508003	09-10-2007
	00036508004	10-10-2007
	00036508005	11-10-2007
MS 1340.7+2859	00036509001	30-05-2007
	00036509002	01-07-2007
MS 1623.4+2712	00036510001	14-11-2007
	00036510002	17-11-2007
MS 2141.2+1730	00036358001	19-04-2007
	00036358002	23-04-2007
	00036511001	09-08-2007
	00036511004	16-10-2007
	00036511005	24-12-2007
	00036511006	11-01-2008
	00036511007	12-01-2008
SDSS J081009.94+384757.0	00036511008	13-01-2008
	00030370001	03-03-2006
MG3 J225155+2217	00036229001	21-12-2007
	00037099001	16-05-2007
	00037099002	21-05-2007
	00037099003	22-05-2007
RX J1456.0+5048 RGB J1629+401	00036660001	26-05-2007
	00030925001	27-04-2007
	00035022001	20-04-2005
	00035022002	23-05-2005
	00035400001	20-01-2006
	00035022003	22-04-2007
	00035022004	28-04-2007
	00035022005	04-05-2007
	00035022006	12-05-2007
	00035022007	18-05-2007
	00035022008	27-05-2007
	00036549001	26-06-2007
	00036549002	08-01-2008
	00036549003	11-01-2008

Individual spectra from multiple pointings, together with the proper response matrices, were integrated by using the addspec task of FTOOLS. The final count spectra were then rebinned in order to have at least 20–30 counts per energy bin, depending on the available statistics, and spectral fits were performed with simple power-law models and galactic N_{H} . In only three cases additional absorption or a broken power-law fit was required. The average spectral parameters are reported in Table 2.

The sensitivity of the hard X-ray detector BAT (optimized for the 15–150 keV energy band, Barthelmy et al. 2005) is generally insufficient to detect extragalactic sources in short exposures, unless for bright states. Therefore, in order to get meaningful signal-to-noise ratios we combined all the available pointings for a given source. All the shadowgrams from pointings of the same source were binned, cleaned from hot pixels and background (flat-field), and deconvolved. The intensity images were then integrated by using the variance as weighting factor. No detection with sufficient signal-to-noise ratio has been found for any source with the available exposures and upper limits at 3σ (corrected for systematic errors) in two energy bands (20–40 and 40–100 keV) have been calculated (see Table 3).

Data from the optical/ultraviolet telescope UVOT (Roming et al. 2005) were analysed using the uvotmaghist task with source regions of 5 arcsec for optical filters and 10 arcsec for the UV filters, while the background was extracted from a source-free annular region with inner radius equal to 6 arcsec (optical) or 12 arcsec (UV) and outer radius from 30 arcsec to 60 arcsec, depending on the presence of nearby contaminating sources. In the cases of MS 0402.0–3613, SDSS J081009.94+384757.0, RX J1456.0+5048 and MG3 J225155+2217 the presence of a nearby source prevents the use of a background region with annular shape; therefore, a circular source free region with 60 arcsec radius was selected. We added a 10 per cent error in flux (corresponding to about 0.1 mag) to take into account systematic effects. The summary of average magnitudes per filters is reported in Table 4.

3.2 *INTEGRAL*

The hard X-ray (20–100 keV) data on MG3 J225155 + 2217 were obtained from the IBIS/ISGRI detector onboard *INTEGRAL* (Lebrun et al. 2003). They were analysed with the Offline Scientific Analysis (OSA) v. 7.0, whose algorithms for IBIS are described in Goldwurm et al. (2003), using the latest calibration files (v. 7.0.2).

The source was observed serendipitously during the revolutions 316 (2005 May 15–18) and 337 (2005 July 17–20) for a total exposure of 388 ks. The results are reported in Table 3. The joint data from the *INTEGRAL*/ISGRI together with those of *Swift*/XRT, covering an energy range of 0.2–100 keV, can be still fitted with a single power-law model with $\Gamma = 1.41 \pm 0.09$ and additional absorption of $N_{\text{H}}^{\text{c}} = (2.1^{+1.3}_{-1.1}) \times 10^{22} \text{ cm}^{-2}$, to mime the low-energy photon deficit. The fit gives a $\chi^2 = 0.96$ for 50 degrees of freedom. The results are consistent with the values for *Swift*/XRT only, reported in Table 2.

3.3 Two-point spectral indices

Two-point spectral indices $\alpha_{\text{ro}}, \alpha_{\text{ox}}, \alpha_{\text{rx}}$ between fixed radio/optical/X-ray frequencies have been computed for all sources, to facilitate comparison with other samples.

Table 2. *Swift*/XRT measurements. N_{H} (from Kalberla et al. 2005) and N_{H}^{c} are in units of 10^{20} cm^{-2} ; exposure is in ks; Γ_1 indicates the photon index in the case of a single power-law model or the soft photon index in the case of a broken power-law model; for the latter, the columns Γ_2 and E_{break} indicates the hard photon index and the break energy (keV); the flux is in units of $10^{-13} \text{ erg cm}^{-2} \text{ s}^{-1}$.

Source	z	N_{H}	Exposure	N_{H}^{c}	Γ_1	Γ_2	E_{break}	$\chi^2/\text{d.o.f.}$	$F_{2-10 \text{ keV}}$
MS 0152.4+0424	1.132	4.00	10.0		1.5 ± 0.2			0.58/8	9.64
MS 0232.5-0414	1.439	2.26	15.4		1.72 ± 0.08			0.93/25	16.3
MS 0402.0-3613	1.417	0.603	27.7	20 ± 10	1.76 ± 0.09			1.20/29	18.3
MS 0521.7+7918	0.503	6.93	21.5		1.9 ± 0.2			0.53/6	3.70
MS 0828.7+6601	0.329	4.31	9.3		1.3 ± 0.2			0.12/5	9.20
MS 1050.9+5418	0.995	0.891	11.2		1.8 ± 0.4			0.86/4	3.56
MS 1234.9+6651	0.852	1.75	32.8		1.8 ± 0.1			1.37/19	5.49
MS 1340.7+2859	0.905	1.24	12.1		1.6 ± 0.1			0.42/12	11.8
MS 1623.4+2712	0.526	3.25	15.6		1.8 ± 0.2			0.63/10	7.60
MS 2141.2+1730	0.211	7.35	43.0		1.69 ± 0.06			1.67/35	15.9
SDSS J081009.94+384757.0	3.946	4.88	10.6		1.4 ± 0.3			0.28/3	5.39
MG3 J225155+2217	3.668	4.90	23.1	210^{+140}_{-110}	$1.41^{+0.10}_{-0.09}$			1.05/42	31.0
RX J1456.0+5048	0.478	1.60	4.8		2.2 ± 0.1			0.77/25	17.7
RGB J1629+401	0.272	0.977	40.7		$3.4^{+0.7}_{-0.3}$	2.21 ± 0.06	$0.47 \pm^{+0.08}_{-0.05}$	1.15/78	9.36

Table 3. *Swift*/BAT and *INTEGRAL*/ISGRI measurements. Exposures are in ks; fluxes are in units of $10^{-10} \text{ erg cm}^{-2} \text{ s}^{-1}$; upper limits are at 3σ level, after having taken into account systematic errors. The Crab spectrum taken as reference for conversion in physical units can be expressed with a power-law model with $\Gamma = 2.1$ and normalization at 1 keV equal to 9.7 photons $\text{cm}^{-2} \text{ s}^{-1} \text{ keV}^{-1}$ (Toor & Seward 1974).

Source	Exposure	$F_{20-40 \text{ keV}}$	$F_{40-100 \text{ keV}}$
MS 0152.4+0424	10.0	<2.1	<3.8
MS 0232.5-0414	15.9	<2.8	<3.5
MS 0402.0-3613	28.5	<1.7	<2.2
MS 0521.7+7918	22.0	<2.4	<3.1
MS 0828.7+6601	9.6	<3.2	<4.0
MS 1050.9+5418	11.6	<2.6	<3.5
MS 1234.9+6651	32.7	<1.5	<2.1
MS 1340.7+2859	12.4	<2.7	<3.9
MS 1623.4+2712	16.0	<2.5	<3.6
MS 2141.2+1730	44.8	<1.8	<2.2
SDSS J081009.94+384757.0	11.0	<2.4	<3.8
MG3 J225155+2217	26.8	<2.3	<2.9
MG3 J225155 + 2217 ^a	388	0.12 ± 0.03	0.32 ± 0.07
RX J1456.0+5048	5.0	<3.3	<4.9
RGB J1629+401	42.8	<1.3	<2.0

^a *INTEGRAL* observation.

The two-point optical/X-ray spectral index has been calculated according to the formula (Ledden & O'Dell 1985)

$$\alpha_{12} = -\frac{\log(S_2/S_1)}{\log(\nu_2/\nu_1)}, \quad (1)$$

where S_1 and S_2 can be the radio ($\nu_r = 5 \text{ GHz}$), optical (at $\nu_o = 8.57 \times 10^{14} \text{ Hz}$ corresponding to 3501 \AA , U filter) and X-ray (at $\nu_x = 2.42 \times 10^{17} \text{ Hz}$ corresponding to 1 keV) flux densities, respectively. The flux densities have been K -corrected by multiplying for the factor $(1+z)^{\alpha-1}$, where α is the spectral index of $S_\nu \propto \nu^{-\alpha}$. An average spectral index α_r has been used for radio and optical frequencies, with values of $\alpha_r = 0.5$ and $\alpha_o = 1.38$ (Pian & Treves 1993). The α_x and X-ray flux density have been measured from the spectral fitting of *Swift*/XRT data reported in Table 2.

The radio flux densities at 5 GHz have been extracted from NASA/IPAC Extragalactic Database (NED)¹ or from radio catalogues available through HEASARC.² When the 5-GHz flux density was not available (a very few cases), we have extrapolated the requested value from the 1.4-GHz flux density.

The *Swift*/UVOT flux densities have been calculated from the observed magnitudes, dereddened with the A_V from NED and extrapolated to other frequencies by means of the extinction law by Cardelli, Clayton & Mathis (1989), and converted by using the zero-points given in the HEASOFT package.

The derived values are reported in Table 4.

4 SED MODELS

The observed SEDs of all sources were modelled following the theoretical scheme developed by Ghisellini et al. (2002) and also used by Celotti & Ghisellini (2008, hereafter CG08), where a more detailed description can be found.

Briefly, the observed radiation is postulated to originate in a single dissipation zone of the jet, described as a cylinder of cross-sectional radius R and thickness (as seen in the comoving frame) $\Delta R' = R$. We assume a conical jet with aperture angle $\psi_j = 0.1$, the dissipation is assumed to always occur at $R_{\text{diss}} = 10 R$.

The relativistic particles are assumed to be injected throughout the emitting volume for a finite time $t'_{\text{inj}} = \Delta R'/c$ with total injected power in relativistic particles L'_{inj} in the comoving frame of the emission region. The observed SED is obtained from the particle distribution resulting from the cumulative effects of the injection and radiative energy loss processes at the end of the injection, at $t = t'_{\text{inj}}$, when the emitted luminosity is maximized.

The finite injection duration, together with the magnetic and radiation energy densities seen by the particles, determine the energy γ_c above which the injected particle spectrum is affected by the radiative cooling processes.

¹ <http://nedwww.ipac.caltech.edu/>.

² <http://heasarc.gsfc.nasa.gov/>.

Table 4. *Swift*/UVOT magnitudes (lower limits are at 3σ level) and the corresponding broad-band spectral indices α_{ro} , α_{ox} and α_{rx} . These have been calculated by using the *K*-corrected fluxes at (3501 Å), 1 keV and 5 GHz. See Section 3.3 for more details.

Source	<i>V</i>	<i>B</i>	<i>U</i>	<i>UVW1</i>	<i>UVM2</i>	<i>UVW2</i>	α_{ro}	α_{ox}	α_{rx}
MS 0152.4+0424	18.6 ± 0.2	19.2 ± 0.2	18.5 ± 0.1				0.61	1.05	0.75
MS 0232.5−0414	16.6 ± 0.1	16.7 ± 0.1	15.5 ± 0.1				0.43	1.29	0.70
MS 0402.0−3613	17.5 ± 0.1	17.7 ± 0.1	16.6 ± 0.1				0.60	1.01	0.74
MS 0521.7+7918	17.1 ± 0.1	17.4 ± 0.1	16.6 ± 0.1				0.38	1.48	0.73
MS 0828.7+6601	>19.7	>20.5	>20.3				<0.77	<0.91	0.81
MS 1050.9+5418	19.3 ± 0.3	19.8 ± 0.3	18.7 ± 0.1				0.57	1.01	0.71
MS 1234.9+6651	17.7 ± 0.1	18.2 ± 0.1	17.2 ± 0.1				0.48	1.22	0.71
MS 1340.7+2859	16.7 ± 0.1	17.1 ± 0.1	16.0 ± 0.1				0.39	1.34	0.69
MS 1623.4+2712	18.8 ± 0.2	18.9 ± 0.1	18.2 ± 0.2				0.60	1.05	0.75
MS 2141.2+1730	16.2 ± 0.1	16.4 ± 0.1	15.2 ± 0.1		15.1 ± 0.1	15.0 ± 0.1	0.49	1.56	0.83
SDSS J081009.94+384757.0	>18.5	>19.4	>19.2	>18.7	>18.9	>19.5	<0.34	<1.03	0.56
MG3 J225155+2217			19.3 ± 0.1	18.9 ± 0.2	18.4 ± 0.1	18.5 ± 0.1	0.52	0.74	0.59
RX J1456.0+5048	18.6 ± 0.3	19.2 ± 0.2	18.4 ± 0.2	17.9 ± 0.2	17.9 ± 0.2	17.9 ± 0.1	0.42	0.69	0.55
RGB J1629+401	17.9 ± 0.2	18.2 ± 0.2	17.2 ± 0.1	16.8 ± 0.1	16.5 ± 0.1	16.5 ± 0.1	0.35	1.26	0.66

The particle injection function is assumed to extend from $\gamma = 1$ to γ_{max} , with a broken power-law shape with slopes $\propto \gamma^{-1}$ and $\propto \gamma^{-s}$ below and above γ_{inj} .

If $\gamma_c < \gamma_{\text{inj}}$ (fast cooling regime) the resulting particle spectrum $N(\gamma)$ is given by

$$N(\gamma) \propto \gamma^{-(s+1)}; \quad \propto \gamma^{-2}; \quad \propto \gamma^{-1}; \quad (2)$$

$$\gamma > \gamma_{\text{inj}}; \quad \gamma_c < \gamma < \gamma_{\text{inj}}; \quad \gamma < \gamma_c.$$

In the opposite case (slow cooling regime), radiative losses affect the spectral shape only at higher energies $\gamma > \gamma_c > \gamma_{\text{inj}}$, yielding

$$N(\gamma) \propto \gamma^{-(s+1)}; \quad \propto \gamma^{-s}; \quad \propto \gamma^{-1}; \quad (3)$$

$$\gamma > \gamma_c; \quad \gamma_{\text{inj}} < \gamma < \gamma_c; \quad \gamma < \gamma_{\text{inj}}.$$

The relativistic electrons radiate via the synchrotron and the inverse Compton (IC) mechanisms. The latter includes the SSC and the external Compton (EC) processes. The external radiation for the EC process is assumed to derive from the accretion disc emission scattered and reprocessed in the surrounding broad line region (BLR) (Sikora, Begelman & Rees 1994).

With the distributions given above, the synchrotron and IC peaks in the SED are due to electrons with Lorentz factor, γ_{peak} , determined by the injected distribution and the radiative losses: in the fast cooling regime $\gamma_{\text{peak}} = \gamma_{\text{inj}}$ as long as $\gamma_{\text{inj}} > 1$. When $\gamma_{\text{inj}} = 1$, $\gamma_{\text{peak}} = \gamma_c$ (provided that $s < 3$). In the slow cooling regime, instead, $\gamma_{\text{peak}} = \gamma_c$ (if $s < 3$).

In most of the sources considered here the data indicate the presence of a prominent optical/UV excess that one can identify with the disc emission and then can be used to estimate L_{disc} . The disc emission is assumed to be a blackbody, peaking at frequency $\nu_{\text{ext}} \sim 10^{15}$ Hz. Besides this blackbody UV component, we also consider the emission of the X-ray corona. This X-ray component is assumed to have $\alpha_x = 1$, to start a factor of 30 below the UV bump, and to have an exponential cut-off at 150 keV. When no optical/UV excess is apparent we still include a possible accretion disc (that can be considered as an upper limit). The external radiation field is derived assuming for the BLR a luminosity $L_{\text{BLR}} = 0.1L_{\text{disc}}$ and a size R_{BLR} derived from the relation

$$R_{\text{BLR}} \sim 10^{17} L_{\text{disc},45}^{1/2} \text{ cm}, \quad (4)$$

where $L_{\text{disc}} = 10^{45} L_{\text{disc},45} \text{ erg s}^{-1}$, in approximate agreement with Kaspi et al. (2007). Since $U_{\text{BLR}} = L_{\text{BLR}}/(4\pi R_{\text{BLR}}^2 c)$, the radiation

energy density of the BLR photons, as measured by an observer inside the BLR at rest with respect to the black hole, is constant, and equal to $U_{\text{BLR}} \sim 0.026 \text{ erg cm}^{-3}$. In the comoving frame, however, the radiation energy density will be enhanced by a Γ^2 factor. When R_{BLR} is smaller than the dissipation zone R_{diss} , we completely neglect any external radiation.

The essential parameters of the model and their role can summarized as follows.

- (i) R, L'_{inj}, s and γ_{inj} determine the injected relativistic particle distribution.
- (ii) The magnetic field B and the radiation energy density U_{rad} determine γ_c , the energy of the cooling break, and thus the particle spectrum after cooling. U_{rad} includes the contribution of both the synchrotron photons and the external photons. In the comoving frame $U'_{\text{ext}} \sim \Gamma^2 U_{\text{ext}}$, therefore also the bulk Lorentz factor Γ is involved.
- (iii) The viewing angle θ , together with Γ , determines the Doppler (beaming) factor δ , and then the boosting of the entire SED.
- (iv) The ratio $\Gamma^2 U_{\text{ext}}/B^2$ determines the EC to synchrotron luminosity ratio.

The SED peak frequencies ($\nu_{\text{peak},S}, \nu_{\text{peak},IC}$) depend mainly on the shape of the particle spectrum. If γ_c is high (low cooling) $\gamma_{\text{peak}} > 10^4$ and $\nu_{\text{peak},S}$ is above the optical band and the SSC dominates the high-energy emission. If γ_c is low (strong cooling) $\gamma_{\text{peak}} < 10-100$ and then $\nu_{\text{peak},S}$ is very much below the optical band, often below the self-absorption frequency, and the EC mechanism produces the high-energy component.

Finally, the power carried by the jet in different forms (radiation, magnetic field, relativistic electrons, cold protons) can be computed from the model parameters as

$$L_i \simeq \pi R^2 \Gamma^2 \beta c U_i, \quad (5)$$

where $U_{\text{rad}} = U'_{\text{rad}}, U_B = B^2/8\pi, U_e = n_e < \gamma > m_e c^2, U_p = n_p m_p c^2$.

We refer to CG08 for a recent estimate and discussion of the jet powers for a large number of blazars.

5 RESULTS

5.1 The EMSS sample

In all cases the X-ray spectra are well fitted by simple power laws with photon indices ranging from 1.8 to 1.3 and the α_{ox} index, which indicates the relative intensity of the X-ray to optical emission, varies from 0.9 to 1.6. None of the objects is detected in the hard X-rays with BAT.

In radio-quiet AGN, where the optical as well as X-ray emission derive from an accretion disc, this ratio is on average $\alpha_{\text{ox}} \simeq 1.6$ (see e.g. Vignali, Brandt & Schneider 2003). Thus, the lower values of α_{ox} for the EMSS sample, i.e. the high ratios of X-ray to optical fluxes (see Table 4) point to a significant contribution from the jet in the X-ray band. This conclusion is reinforced by the derived spectral indices in the X-ray band ($\alpha_x \simeq 0.3\text{--}0.7$) which are unusually hard for normal, even radio-loud but not flat-spectrum quasars ($\alpha_x \simeq 0.8\text{--}1$, see Grandi, Malaguti & Fiocchi 2006; Guainazzi et al. 2006). Therefore, the observed X-ray emission can be attributed to the combined contributions from the accretion disc corona plus a harder X-ray component deriving from IC scattering of external photons (EC) off relativistic electrons in the jet. We recall that all the objects in the sample have BLRs providing seeds for the EC process.

The optical and X-ray fluxes derived from *Swift* for the 10 X-ray-selected radio-loud AGN are shown in Fig. 1 (in order of redshift), together with historical radio and optical data, and theoretical models for the full SEDs. The high optical/UV fluxes and hard X-ray spectra indicate that the UV to X-ray SED have a concave shape as commonly observed for FSRQs. Therefore, in all cases the synchrotron peak frequency should fall below the UV range (red SED). On the other hand, the lack of data in the IR–submillimetre region does not allow us to set stronger observational constraints on its location.

It is noteworthy that the two objects with the highest α_{ox} , MS 2141.2+1730 and MS 0521.7+7918, have relatively low radio luminosity ($\approx 10^{42}$ erg s $^{-1}$). This suggests that the jets in these sources could be either intrinsically weak or seen at intermediate angles, therefore not strongly beamed (see also Landt et al. 2008). Indeed, the unified model predicts that blazars at intermediate angle should exist (in large numbers). Sources with subluminal jets were not present in the samples used to construct the sequence, likely because the high threshold in radio flux selected only the most beamed sources.

The X-ray-selected AGN considered here, whose radio emission was in some sense measured ‘a posteriori’, have radio fluxes on average around 200 mJy and radio luminosities in the range $10^{42}\text{--}10^{44}$ erg s $^{-1}$, about one order of magnitude lower than the range

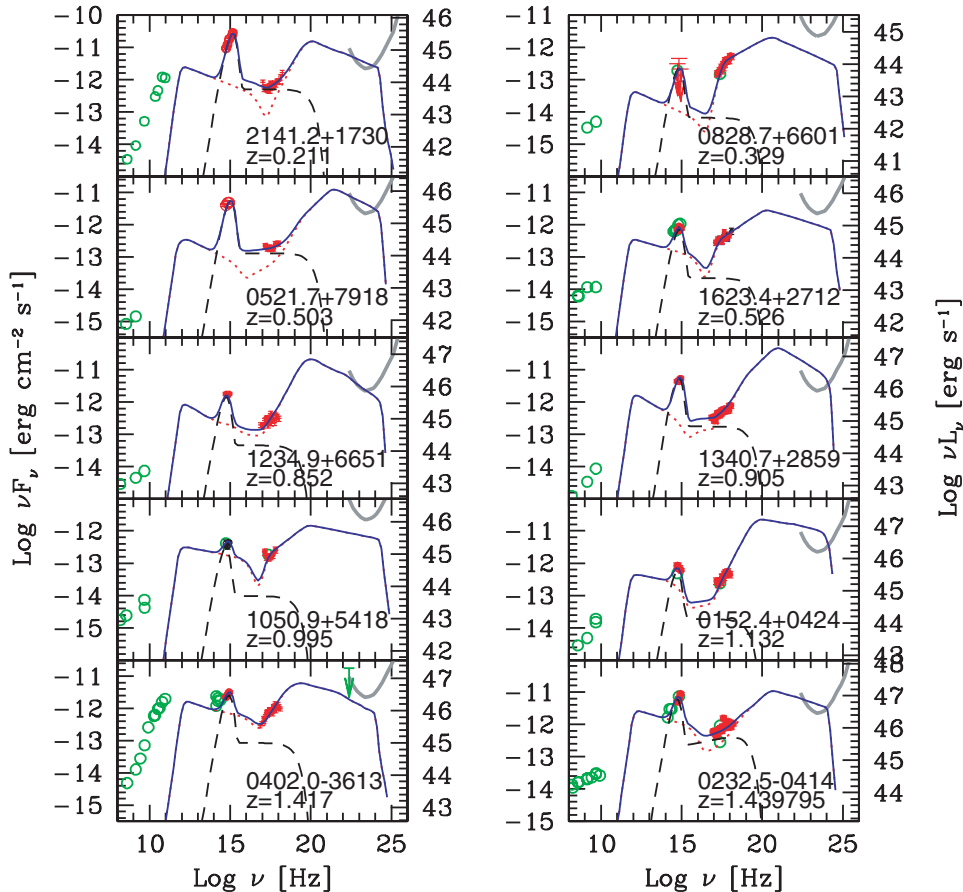


Figure 1. SEDs of the 10 EMSS blazars in our sample, shown in order of increasing redshift. The models include the contribution of a putative accretion disc (dashed lines) described by a blackbody component peaking at $\sim 10^{15}$ Hz plus a power-law component in X-rays produced by a hot corona. The non thermal jet emission (dotted lines) is due to synchrotron radiation (self-absorbed at millimetre wavelengths) and IC scattering of photons in the BLR (see text). The solid lines represent the total emission. Light grey symbols (green in the electronic version) refer to archival data (taken from NED), darker symbols (red in the electronic version) represent the data analysed in this paper. The grey line indicates the expected flux sensitivity (5σ , 1 yr of exposure) of the FGRT.

Table 5. The input parameters of the model for our blazars. (1) Source name; (2) redshift; (3) radius R of emitting region (10^{15} cm); (4) intrinsic injected power (10^{45} erg s $^{-1}$); (5) bulk Lorentz factor; (6) viewing angle; (7) magnetic field intensity (G); (8) minimum random Lorentz factor of the injected particles; (9) maximum random Lorentz factor of the injected particles; (10) γ_{peak} ; (11) spectral slope of particles above the cooling break; (12) disc luminosity (10^{45} erg s $^{-1}$); (13) radius of the BLR (10^{15} cm); (14) random Lorentz factor of the electrons cooling in $\Delta R'/c$.

Source (1)	z (2)	R (3)	L'_{inj} (4)	Γ (5)	θ (6)	B (7)	γ_{inj} (8)	γ_{max} (9)	γ_{peak} (10)	n (11)	L_d (12)	R_{BLR} (13)	γ_c (14)	Note (15)
MS 0152.4+0424	1.132	10	1.5e-2	14	3.3	2.4	1	3e3	18	3.2	5	220	11	
MS 0232.5-0414	1.439	18	3.0e-2	13	4.0	7	1	6e3	50	3.3	100	1.e3	6	
MS 0402.0-3613	1.417	12	2.3e-2	11	4.0	8	4	1e4	11	3.4	40	700	11	
MS 0521.7+7918	0.503	10	1.0e-2	13	6.0	2	150	8e3	150	3.5	7	300	18	
MS 0828.7+6601	0.329	2	6.0e-5	14	3.2	3	1	1e4	37	3.45	0.1	25	37	
MS 1050.9+5418	0.995	10	1.5e-3	12	3.5	5	1	1e4	21	3.2	2	180	21	$R_{\text{diss}} < R_{\text{BLR}}$
		18	2.5e-3	12	3.5	0.12	400	2e5	7e3	3.5	2	140	7e3	$R_{\text{diss}} > R_{\text{BLR}}$
MS 1234.9+6651	0.852	9	7.0e-3	12	3.5	3	15	5e3	25	3.6	6.5	320	25	
MS 1340.7+2859	0.905	14	2.5e-2	13	4.0	3	70	3e3	70	3.6	29	500	8	L_γ below <i>GLAST</i>
		14	2.0e-2	14	4.5	5	40	3e3	40	3.7	25	550	9	L_γ above <i>GLAST</i>
MS 1623.4+2712	0.526	10	1.6e-3	11	5.0	3	1	1e4	37	3.3	1	150	37	$R_{\text{diss}} < R_{\text{BLR}}$
		15	3.6e-4	11	3.5	0.1	300	1e4	2.1e4	3.6	1	100	2e4	$R_{\text{diss}} > R_{\text{BLR}}$
MS 2141.2+1739	0.211	10	9.0e-4	12	5.0	6.5	20	1.5e4	20	2.4	4.5	200	12	
SDSSJ081009.94+384757.0	3.946	16	0.1	14	3.0	5	25	1.5e3	25	3.8	100	1000	6	
MG3 J225155+2217	3.668	20	0.2	15	2.5	0.7	35	1e3	35	3.8	21	500	6	
RX J1456.0+5048	0.478	15	2.0e-4	15	3.0	0.3	3.5e4	5e5	3.5e4	3.4	0.2	45	1e4	$R_{\text{diss}} > R_{\text{BLR}}$
RGB J1629+401	0.272	10	1.1e-4	10	4.0	1.5	7e3	1e5	7e3	3.5	0.25	50	930	$R_{\text{diss}} > R_{\text{BLR}}$

covered by the FSRQs in the sequence. The optical fluxes, indicative of the accretion disc emission, correspond instead to luminosities of 10^{45} – 10^{47} erg s $^{-1}$, well in to the typical quasar range. An even lower radio power interval was explored by Caccianiga & Marcha (2004), though without spectral information.

MS 0828.7+6601 is extreme in the opposite way, in that the optical luminosity is lower than the X-ray one and the X-ray spectrum is extremely hard ($\alpha_x = 0.3$). The Galactic absorption column is $N_H = 4.31 \times 10^{20}$ cm $^{-2}$ and the X-ray spectrum does not show any hint of additional absorption, suggesting that the source is intrinsically faint at optical wavelengths.

The SED models shown in Fig. 1 (continuous/blue lines) were computed as described in Section 3. As noted above the main observational constraints are that the synchrotron peak should fall below the UV range and that the jet contribution in X-rays should have a hard slope. Observational data below the optical and above the X-ray range are lacking so that the models cannot be more strongly constrained. According to our SED models the peak of the high-energy emission, always dominated by the EC process, falls around 1–10 MeV, unusually low compared to known γ -ray blazars. γ -ray observations would be extremely important to confirm these models: the sensitivity curve of the Fermi GRT, for a 1-yr exposure, shown for comparison on each SED, indicates that several of these sources may be detected in the near future.

The model parameters adopted are reported in Table 5.

Since the lack of high-energy (hard X-ray and γ -ray) data leaves some freedom in the choice of the fitting parameters we present also examples of alternative models for the SEDs.

In Fig. 2 two models for the SED of MS 1340.7 + 2859, both fitting the optical and X-ray data equally well, are compared. The first (same as in Fig. 1) predicts a γ -ray flux well above the Fermi-GRT sensitivity; the second predicts a lower γ -ray flux, just below the FermiGRT sensitivity limit. The parameters for the two models are quite similar (see Table 5).

In Fig. 3 alternative SED models (solid lines) for MS 1050.9+5413 and MS 1623.4+2712 are shown. Both sources are

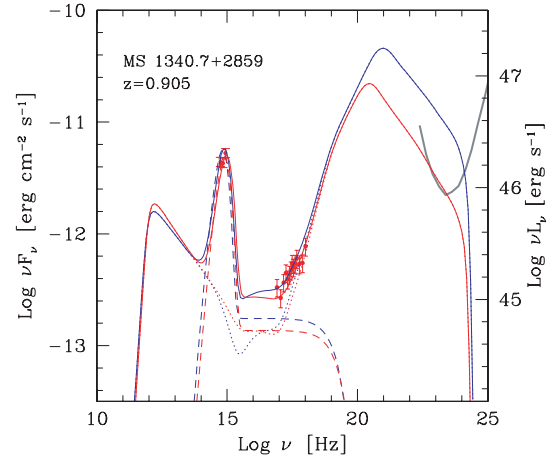


Figure 2. SEDs of MS 1340.7+2859, together with two possible fits. The one with the high-energy emission above the *GLAST* detection curve (blue line), is the same as in Fig. 1. The parameters for the two fits, listed in Table 5, differ only slightly, but the predicted flux in the *GLAST* band is quite different.

characterized by a relatively small accretion disc luminosity, hence a small R_{BLR} , a ‘normal’ X-ray to optical luminosity ratio and a ‘normal’ X-ray slope (as opposed to e.g. MS 0828.7+6601, which has a relatively stronger, and harder, X-ray component). We hypothesize here that the dissipation region of the jet is beyond the BLR (i.e. $R_{\text{diss}} > R_{\text{BLR}}$), contrary to what assumed for the models shown in Fig. 1. Then, in the absence of external photons, the cooling threshold γ_c is high and the synchrotron emission peaks close to (but not above) the optical band, while the whole high-energy emission from X-rays to γ -rays is produced by the SSC (instead of EC) process. Note that the injection spectrum is also different from the previous models, in that γ_{inj} changes from 1 to 400 and 300 for the two sources, respectively (see Table 5). As a consequence the

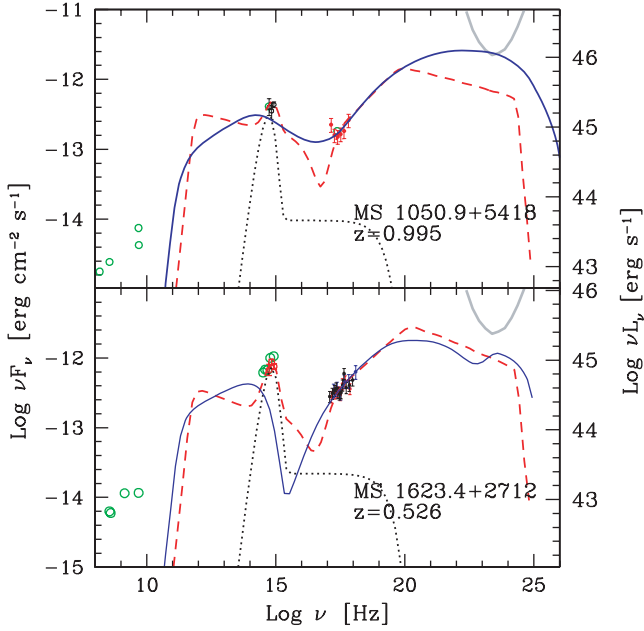


Figure 3. SED of MS 1050.9+5418 and MS 1623.4+2712 together with two possible fits. For both sources the dashed line is the same fit as in Fig. 1. The solid line, instead, corresponds to assuming that the emission region is beyond the radius of the BLR. Consequently, the EC process is completely neglected. This corresponds to less radiative cooling and a larger γ_{peak} , and in turn this corresponds to a synchrotron peak at much larger frequencies. In this case, the high-energy flux is completely due to the SSC process.

jet powers computed for the latter models are significantly reduced (Table 6).

These examples illustrate the ambiguities in our models when α_x and α_{ox} are ‘normal’, and the accretion disc luminosity is relatively modest, suggesting a small BLR. It is clear from Fig. 3 that additional data, especially between the submillimetre and the optical region of the SED are needed to discriminate between these alter-

natives. In the following we discuss the results assuming in all the cases the parameters obtained with the standard EC model.

5.2 Controversial blazars

5.2.1 Two high-redshift ‘red’ blazars

Two high-redshift powerful blazars recently discovered (SDSS J081009.94+384757.0, Giommi et al. 2007b; Falco, Kochanek & Munoz 1998; MG3 J225155+2217, Bassani et al. 2007), both showing conspicuous broad lines, have been claimed to possibly exhibit a *synchrotron peak* in the X-ray band at variance with the sequence scheme. Our reanalysis of all the existing *Swift* and *INTEGRAL* data is summarized in the tables and the results are shown in Fig. 4. For SDSS J081009.94+384757.0 the *Swift* observations yield only upper limits in the optical UV range. Therefore the optical fluxes measured by the Sloan Digital Sky Survey (SDSS), though not simultaneous to the X-ray data, are also shown in Fig. 4. In both cases the hard X-ray spectra suggest a concavity of the optical to X-ray SEDs, pointing to an IC origin of the X-ray/hard X-ray emission. Though both objects have $\alpha_{\text{rx}} \simeq 0.6$, less than the conventional threshold value of 0.78 taken to distinguish ‘high-energy-peaked’ BL Lacs (HBL) from ‘low-energy-peaked’ BL Lacs (LBL), the ‘red’ nature of their SEDs seems clear even with these limited data.

The case of MG3 J225155+2217 discovered with *INTEGRAL* is extraordinary: the X-ray to hard X-ray component dominates the optical emission by more than one order of magnitude. Attributing the latter component to synchrotron emission would require implausibly high values of both magnetic field and particle energies. The SED of this source is very similar to that of *Swift* J0746.3+2548 ($z = 2.979$) discovered by the BAT instrument on board *Swift* (Sambruna et al. 2006a).

Clearly, a hard X-ray selection favours the discovery of objects with an extremely dominant hard X-ray component. It is nevertheless interesting that blazars with such extreme dominance of the high-energy emission component actually exist.

Our model SEDs are shown in (Fig. 4) For SDSS J081009.94+384757.0, although the wavelength coverage is poor,

Table 6. Kinetic powers and Poynting fluxes (all in units of $10^{45} \text{ erg s}^{-1}$) – (1) source name; (2) total (synchrotron + IC) radiative power L_r ; (3) synchrotron radiative power L_s ; (4) poynting flux L_B ; (5) kinetic power in emitting electrons L_e ; (6) kinetic power in protons L_p , assuming one proton per electron; (7) average random electron Lorentz factor $\langle\gamma\rangle$.

Source (1)	L_r (2)	L_s (3)	L_B (4)	L_e (5)	L_p (6)	$\langle\gamma\rangle$ (7)	Note (8)
MS 0152.4+0424	3.15	0.04	0.42	1.11	253	8.1	
MS 0232.5–0414	4.92	0.73	10.03	0.68	152	8.2	
MS 0402.0–3613	2.29	0.33	4.16	2.90	1301	4.1	
MS 0521.7+7918	1.73	0.04	0.25	0.29	31	17.6	
MS 0828.7+6601	$1.20\text{e-}2$	$1.53\text{e-}4$	$2.64\text{e-}2$	$3.24\text{e-}2$	21	2.9	
MS 1050.9+5418	0.20	$2.67\text{e-}2$	1.25	0.24	129	3.4	$R_{\text{diss}} < R_{\text{BLR}}$
	0.39	$2.90\text{e-}2$	$2.51\text{e-}3$	1.27	14.4	162	$R_{\text{diss}} > R_{\text{BLR}}$
MS 1234.9+6651	1.02	$2.71\text{e-}2$	0.39	1.10	236	8.6	
MS 1340.7+2859	4.32	$9.73\text{e-}2$	1.11	0.78	142	10	L_γ below GLAST
	3.80	0.195	3.59	1.22	254	8.8	L_γ above GLAST
MS 1623.4+2712	0.19	$1.50\text{e-}2$	0.41	3.66	203	3.3	$R_{\text{diss}} < R_{\text{BLR}}$
	$5.60\text{e-}2$	$6.0\text{e-}3$	$1.0\text{e-}3$	0.96	15	117	$R_{\text{diss}} > R_{\text{BLR}}$
MS 2141.2+1739	0.12	$1.38\text{e-}2$	2.27	$5.52\text{e-}2$	12.4	8.2	
SDSS J081009.94+384757.0	19.79	0.44	4.69	7.10	1996	6.5	
MG3 J225155+2217	50.05	$2.12\text{e-}2$	0.16	12.77	3320	7	
RX J1456.0+5048	$3.26\text{e-}2$	$2.13\text{e-}2$	$1.70\text{e-}2$	$1.17\text{e-}2$	$7.1\text{e-}3$	3049	$R_{\text{diss}} > R_{\text{BLR}}$
RGB J1629+401	$1.13\text{e-}2$	$1.03\text{e-}2$	$8.39\text{e-}2$	$2.23\text{e-}3$	$9.3\text{e-}3$	442	$R_{\text{diss}} > R_{\text{BLR}}$

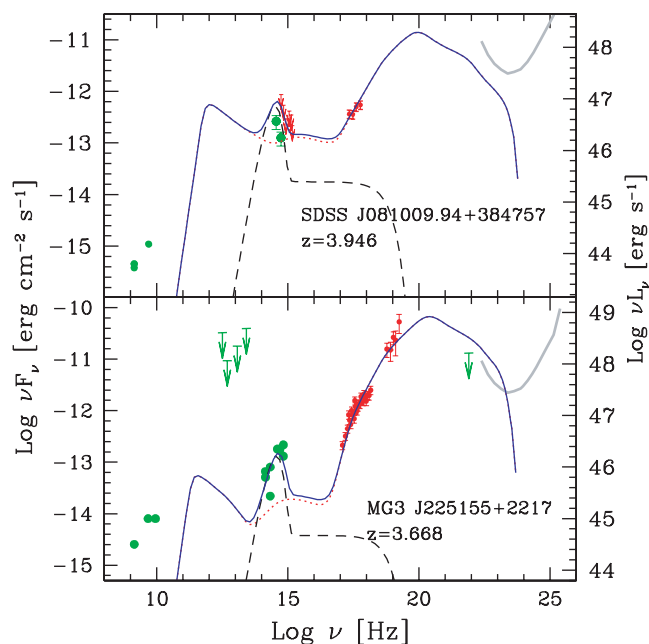


Figure 4. SEDs of the two high-redshift blazars: MG3 J225155+2217 and SDSS J081009.94+384757.0. Same symbols as in Fig. 1.

the hard X-ray spectrum measured by *Swift* strongly disfavours both a synchrotron and SSC interpretation of the X-ray emission. We therefore propose a model with synchrotron peak at low energies and a strong EC component. On the other hand the peak energy of the EC component is uncertain as in the case discussed above for MS1340.7.

For MG3 J225155+2217 the *INTEGRAL* data define well the lower energy side of the EC component: this branch of the SED reveals the low-energy end of the electron distribution. The SED model is sufficiently determined by the data and the peak energy of the EC component is unlikely to be higher.

5.2.2 Two luminous ‘blue’ blazars

The SEDs for RX J1456.0+5048 and RGB J1629+401 including all the data analysed here, are shown in Fig. 5. Here the data confirm the ‘blue’ nature of the SEDs as discussed already in Padovani et al. (2002) and Giommi (2008), respectively. In both cases the synchrotron peak falls in the UV to X-ray range as typical for HBL.

Indeed RX J1456.0+5048 can be classified as a BL Lac, since its optical spectrum from the SDSS (see Fig. 6) shows a blue continuum and very weak emission lines, with equivalent width $< 5 \text{ \AA}$.³ We note also that the radio source previously associated with this object is probably a misidentification: a bright, compact flat-spectrum radio source in the field, about 44 arcsec to the east of the SDSS BL Lac object, dominates the radio flux in this region. In the best image from the FIRST, at 1.4 GHz, the field source is 168 mJy, whereas the BL Lac object is only 9.5 mJy (T. Cheung, private communication). The latter value for the radio flux is shown in Fig. 5. RX J1456.0+5048 is highly luminous, but still comparable to the well-known HBL

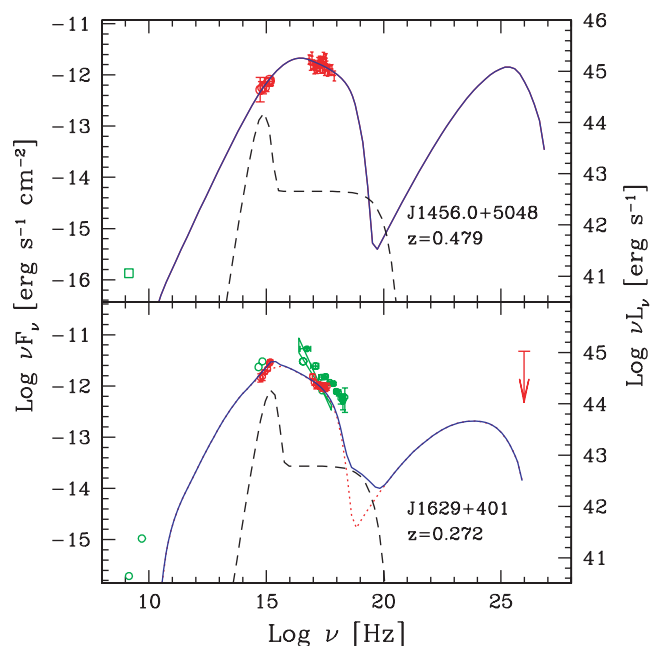


Figure 5. SEDs of the two ‘blue’ blazars with emission lines, RX J1456.0+5048 and RGB J1629+401. The plotted disc and corona spectra should be considered as an upper limit to the thermal emission in these blazars. Since the dissipation region is beyond the location of the BLR, their photons so not contribute to the IC spectra.

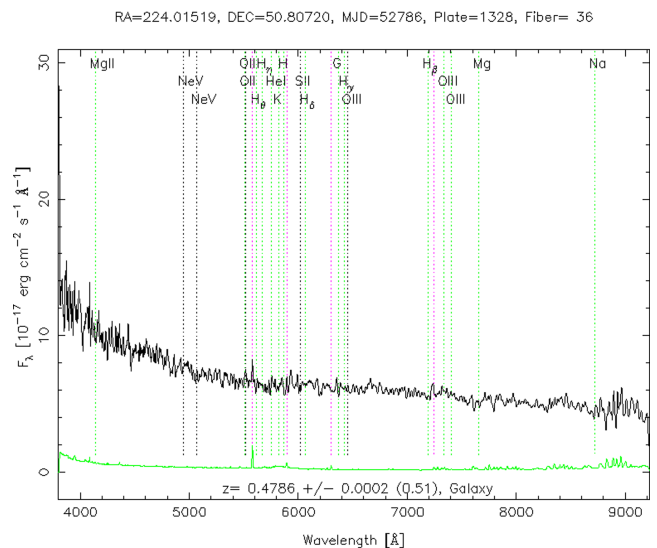


Figure 6. Optical spectrum of RX J1456.0+5048 from the SDSS.

PKS 2155–304 in the bright state recently observed (Foschini et al. 2007, 2008).

The SED model for this object shown in Fig. 5 formally assumes $R_{\text{diss}} > R_{\text{BLR}}$; however, there is no indication that a BLR exists at all in this object. Also the possible contribution of an accretion disc is only an upper limit. The cooling threshold γ_c is very high, as well as the break energy of the injection spectrum γ_{inj} which coincides with γ_{peak} .

The case of RGB J1629+401 is intriguing. Its optical spectrum, also from the SDSS, is shown in Fig. 7. The emission lines are pronounced, but ‘narrow’ (FWHM $< 1500 \text{ km s}^{-1}$, Komossa et al.

³ According to the line measurements available in the SDSS server at <http://cas.sdss.org/astrodr6/en>.

RA=247.25546, DEC=40.13331, MJD=52759, Plate=1172, Fiber=607

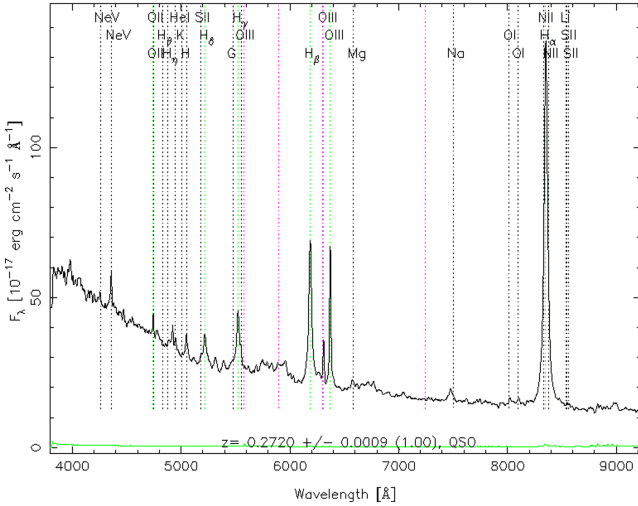


Figure 7. Optical spectrum of RGB J1629+401 from the SDSS.

2006), typical of narrow-line Seyfert 1 (NLSy1) galaxies. Estimates of the mass of the central BH are in the range $2 \times 10^7 M_\odot$ (Komossa et al. 2006). This is unusual for a radio-loud source and in particular for blazars. However, mass estimates for NLSy1 galaxies may have to be revised (Decarli et al. 2008; Marconi et al. 2008). In fact the whole case of NLSy1 and particularly that of radio-loud NLSy1 is the subject of active debate (e.g. Malizia et al. 2008; Yuan et al. 2008). Specifically RGB J1629+401 is only moderately radio-loud and its X-ray emission spectrum showing a broken power-law spectrum with spectral indices $\Gamma_1 = 3.4^{+0.7}_{-0.3}$ and $\Gamma_2 = 2.21 \pm 0.06$ below and above 0.5 keV does not point unambiguously to a jet contribution. The X-ray emission could be driven by its NLSy1 nature (Komossa et al. 2006).

Nevertheless we modelled the SED of this source assuming a jet contribution and negligible radiative losses in the dissipation region ($R_{\text{diss}} > R_{\text{BLR}}$). The radiation energy density is thus due to magnetic field and synchrotron photons only. The resulting SSC component has low luminosity.

The parameters derived modelling the observed SEDs for all the objects are given in Table 5. The powers carried by the jets in various forms, derived from the models, are reported in Table 6.

6 DISCUSSION

6.1 Model parameters and correlations

It is interesting to compare the (model-independent) two-point spectral index α_{ox} with quantities derived from the modelling for the EMSS sample. α_{ox} describes the ratio of the optical to X-ray emission. For the ‘red’ SEDs of this sample the optical is often dominated by the accretion disc emission while the X-ray contribution in excess of the accretion disc corona can derive from the jet, therefore α_{ox} is a measure of their relative strength.

We find from the modelling that α_{ox} correlates with the viewing angle θ (Fig. 8) as well as (inversely) with the Doppler factor δ (not shown). We recall that Γ and δ enter the models in different ways so that both are determined in the fits: θ is then derived from the first two. The two correlations are not independent as the value of Γ is almost constant ranging between 10 and 15.

The $\alpha_{\text{ox}}-\theta$ correlation agrees with the initial expectation that relatively weak jet contributions could derive from intermediate

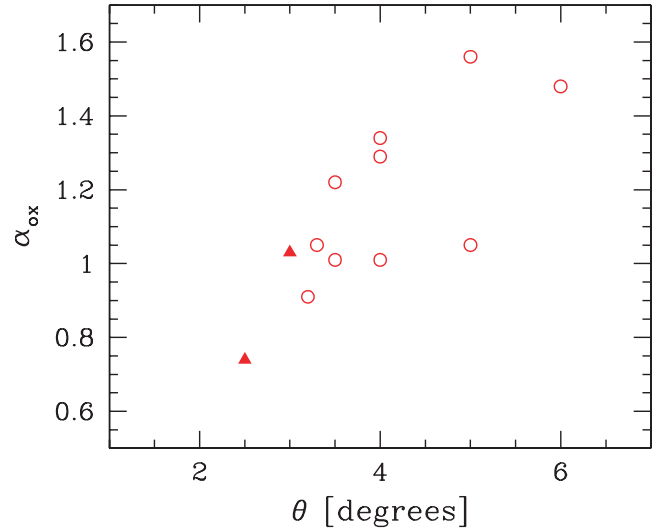


Figure 8. The broad-band spectral UV to X-ray spectral index α_{ox} as a function of viewing angle. Filled points are the high- z blazars (triangles).

viewing angles. However, α_{ox} also correlates *inversely* with the estimated jet intrinsic power, so that the two effects, a lower degree of beaming or a lower intrinsic jet power, cannot be disentangled and probably coexist. On the other hand, α_{ox} does not correlate with L_{disc} , indicating that it is the *relative* jet ‘strength’, either due to the viewing angle or to the intrinsic power, that may drive these correlations.

The most important parameter determining the *shape* of the SED is γ_{peak} , the energy of electrons radiating the peak synchrotron luminosity. The relation between γ_{peak} and the radiation energy density as seen in the emission region frame, u_{rad} , is shown in Fig. 9, for the objects discussed here. Values derived for the blazars modelled in CG08 are also shown for comparison. The new objects fall well within the parameter sequence defined by the previous

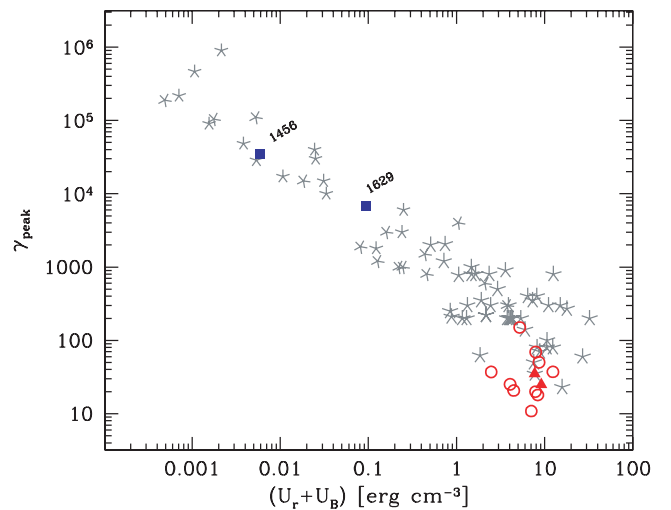


Figure 9. The energy of electrons emitting at the peaks of the SED, γ_{peak} as a function of the energy density (radiative plus magnetic) as seen in the comoving frame. Our EMSS sources are shown as empty circles. The two squares correspond to the two ‘blue’ FSRQs in our sample, while the two filled triangles correspond to the two high-redshift blazars SDSS J081009.94+384757.0 and MG3 J225155+2217. For comparison, we show also all the blazars studied in CG08 (grey asterisks).

sample. Therefore, despite the different selection criteria, X-ray selection as opposed to radio selection for FSRQ and selections aimed at finding sources breaking the sequence trends, the spectral sequence holds in terms of physical parameters.

The ‘red’ objects tend to cluster at one end, with rather low γ_{peak} . The clustering can result from the assumption (adapted from Kaspi et al. 2007) of an almost constant intrinsic radiation energy density in the BLR: since the magnetic field value is limited by the high Compton to synchrotron ratio, $U_{\text{rad}} \simeq U_{\text{BLR}} \Gamma^2$ (which varies by a factor of 2 for Γ between 10 and 15) cannot be exceeded substantially.

Blue SEDs are obtained for small U_{rad} , such that $\gamma_{\text{peak}} = \gamma_c$ is high, while the opposite is true for red SEDs. This is a result of the feedback introduced by including radiative cooling in modelling the energy distribution of the relativistic electrons. However, this is not the only important difference between the electron distributions producing blue and red SEDs. Another major difference is at the lower electron energies: in fact, below γ_{peak} , the assumed electron distribution is extremely hard ($\propto \gamma^{-1}$) so that the total number of electrons is small and their average energy much higher than in the case of red SEDs (see Table 6).

6.2 Jet powers

The total jet power, P_{jet} , computed from the models (see Section 4) is shown versus the luminosity of the accretion disc (estimated from the data) in Fig. 10, together with values previously derived for other blazars (Maraschi & Tavecchio 2003; Sambruna et al. 2006b). The two quantities tend to correlate for the red SEDs. Moreover, the value of P_{jet} is of the order of 10 times the disc luminosity, corresponding to an approximate equality of the jet power and the accretion power (for an assumed radiative efficiency of the accretion process of 10 per cent appropriate for an optically thick flow). This represents on one hand an interesting consistency check on the models. In fact the bulk Lorentz factor, size, magnetic

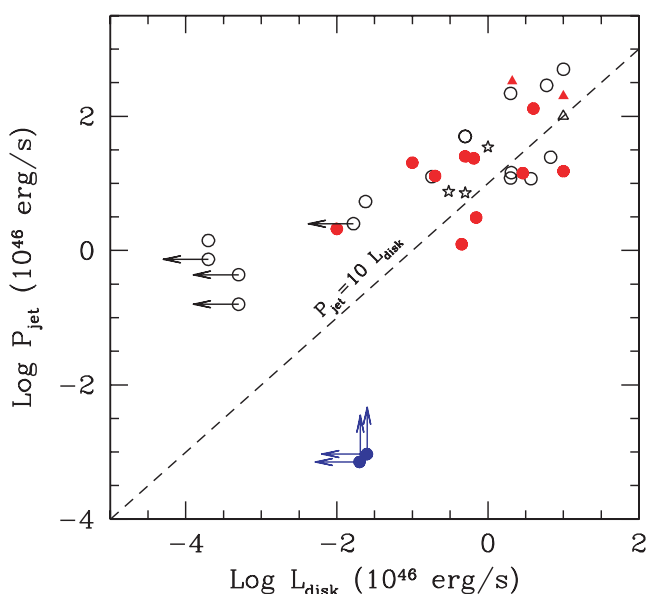


Figure 10. The total jet power as a function of the disc luminosity, for the blazars studied in this paper. Filled red triangles are the high- z blazars and filled blue circles are the ‘blue’ blazars. For comparison, black open symbols report the data obtained for other blazars (Maraschi & Tavecchio 2003; Sambruna et al. 2006b).

field, particle densities and spectra in the dissipation region are chosen to satisfy the SED constraints, including clearly the observed fluxes/luminosities, but the jet power is a global quantity that is computed a posteriori. Moreover, the new data and models increase significantly the number of sources in which a comparison of the jet power with the accretion power is possible and confirms the substantial balance between the two.

The value of the power for jets with red SEDs depends quite strongly on the minimum energy of the injected electrons, γ_{min} , which is often poorly constrained. For red SEDs the X-ray emission derives from the EC process of relatively low-energy electrons thus a lower limit can be obtained. Moreover in several cases, γ_{min} could be inferred from detailed fits of X-ray spectra showing a break in the X-ray range. Such breaks have sometimes been interpreted as absorption by cold gas (e.g. Cappi et al. 1997; Fiore et al. 1998; Fabian et al. 2001a,b; Bassett et al. 2004) but could represent instead the low-energy ‘end’ of the electron distribution (e.g. Tavecchio et al. 2007). With the latter interpretation γ_{min} is found to be in the range 1–10, thus supporting the high power values (Tavecchio et al. 2000; Maraschi & Tavecchio 2003; CG08). These powers rest on the assumption of one cold proton per electron, but are independently required by the fact that the power directly radiated by the jet is larger than the power in relativistic leptons and magnetic field (CG08).

For jets with blue SEDs the jet power derived from the present models is substantially lower, due to the smaller number and higher mean energy of particles in the assumed relativistic electron population. The uncertainty on the amount of low-energy electrons in the jet is however quite large because radiation from this branch of the electron distribution is not observable: its synchrotron emission is covered by the larger fluxes due to the outer regions of the jet and its SSC emission falls in the hard X-ray–soft γ -ray region of the spectrum which is difficult to observe. Note that from Table 6 the total kinetic power from the ‘blue’ jets is hardly sufficient to account for the emitted radiation, thus the assumed spectra lead to a lower limit in the estimate of the jet powers.

As a result, in the $P_{\text{jet}}-L_{\text{disc}}$ plane, the ‘blue’ objects modelled here fall well below the $P_{\text{jet}} = 10 L_{\text{disc}}$ line. In the same diagram the grey open circles with upper limits to the disc luminosities (horizontal arrows) represent BL Lacs from Maraschi & Tavecchio (2003) for which an electron distribution with slope 2 extending down to a Lorentz factor of 1 was assumed below the peak energy.

Despite the large uncertainties about the powers of the ‘blue’ objects, it is interesting that the ‘red’ blazars discussed here which result from independent selection criteria in the X-ray/hard X-ray band confirm the results previously obtained for radio-selected FSRQ.

Very different results were obtained by Nieppola et al. (2008) for a large sample of Blazars using beaming corrections derived from brightness temperatures at high radio frequencies using variability to estimate the sizes of the emission regions. This technique gives information on the Doppler factors for the radio-emitting regions in AGN. They find an anticorrelation between Doppler factor and peak frequency of the synchrotron component such that the objects with higher peak frequency are less beamed. As a result the ‘intrinsic’ powers of objects with large peak frequency (i.e. ‘blue’ objects) are higher than those of ‘red’ objects.

While models of TeV emitting blazars require Doppler factors as large as 10–50 (e.g. Krawczynski, Coppi & Aharonian 2002; Konopelko et al. 2003; Aharonian et al. 2008; Finke, Dermer & Böttcher 2008; Tagliaferri et al. 2008), very long baseline interferometry (VLBI) observations show very small, subluminal

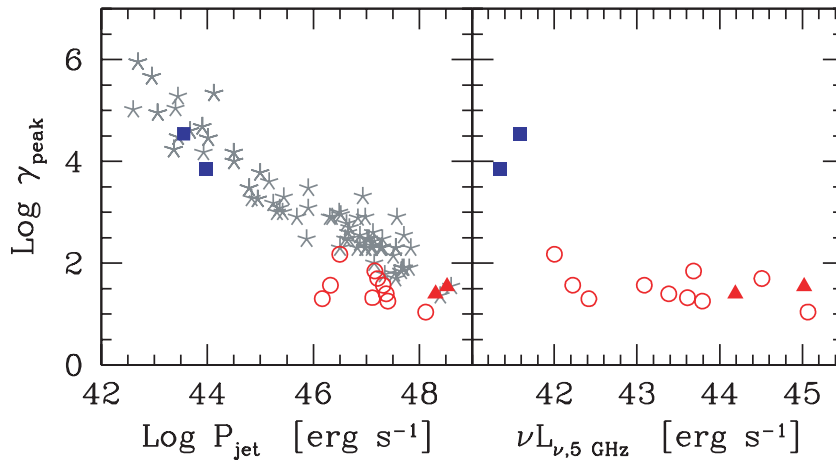


Figure 11. The energy of electrons emitting at the peaks of the SED, γ_{peak} as a function of total jet power (left-hand panel, for comparison in grey data from CG08) and the radio luminosity at 5 GHz (right-hand panel). Symbols are as in Fig. 9. A ‘sequence’ (i.e. correlation) is still apparent between γ_{peak} and P_{jet} , while γ_{peak} does not show a clear correlation with observed radio luminosity.

motions (e.g. Piner, Pant & Edwards 2008). These two evidences can be reconciled assuming that the jet strongly decelerates from the blazar region to the VLBI scale, from which most of the radio emission originates (Georganopoulos & Kazanas 2003; Ghisellini, Tavecchio & Chiaberge 2005). This would also fit in with the scenario in which Fanaroff–Riley type I (FR I) jets decelerate on moderate scalelengths while FR II jets may remain relativistic up to very large scales (e.g. Tavecchio 2007). Therefore the Doppler factors obtained by Nieppola et al. (2008) for the jet radio-emitting regions are probably much smaller than the Doppler factors in the optical-to- γ -ray emitting region especially in the case of HBL objects.

7 CONCLUSIONS

We have analysed and modelled new data for the SEDs of blazars including the first X-ray-selected sample of radio-loud quasars and a few more blazars claimed to possibly challenge the ‘blazar spectral sequence’. The first, model independent, conclusion is that the conventional separation of different ‘types’ of blazars according to their two-point spectral indices (α_{ro} , α_{ox} , α_{rx}) can be deceiving, due to the complexity and variety of the SEDs: for instance the traditional criterion $\alpha_{\text{rx}} > (<) 0.78$ to distinguish between blue and red SEDs fails in the case of SDSS J081009.94+384757.0 and MG3 J225155+2217 which have $\alpha_{\text{rx}} \simeq 0.6$, yet this is not due to synchrotron emission in the X-ray band but to an extremely dominant Compton component. Results from the Fermi Gamma-ray Telescope will be critical in confirming our interpretation.

The ‘blazar spectral sequence’ concept still holds in terms of a parameter sequence. In Fig. 11 (left-hand panel) the parameter γ_{peak} computed from SED models is plotted versus total jet power also computed from the models. A ‘sequence’ (i.e. correlation) is still apparent between these two quantities. We stress that γ_{peak} is related to the spectral shape while P_{jet} is a global quantity related to the emitted luminosity.

However (Fig. 11, right-hand panel), γ_{peak} does not show a clear correlation with the observed radio luminosity, which was the basic quantity used in building the spectral sequence. This is likely due to the fact that at lower flux thresholds intrinsically luminous but less beamed objects enter the samples causing a mix of lower luminosity due to lower intrinsic power or lower beaming. This ambiguity could probably be solved with high resolution radio observations.

The spectral sequence requires that different ‘types’ of blazars, from FSRQ to LBLs to HBLs, have SED peaks at increasing frequencies. This is accounted for by increasing values of γ_{peak} , derived in our models with the assumption that radiative cooling affects the electron distribution becoming less important as the radiation energy density around the dissipation region decreases. However, the particle distributions needed to account for red and blue SEDs, respectively, differ not only at the high-energy end but also at the low-energy end. Blue SEDs require an electron population with higher ‘average’ energy, perhaps pointing to different injection/acceleration mechanisms.

The present results show that even X-ray selection does not lead to find ‘blue’ quasars as was the case for X-ray-selected BL Lac samples (see also Landt et al. 2008). This strengthens the conclusion that when a bright accretion disc is present the SED is always ‘red’. However, if the initial samples suggested luminosity/power as a fundamental parameter in determining the SEDs’ systematics, the present study suggests that the fundamental condition that separates ‘red’ SEDs from ‘blue’ ones is the intensity of the radiation field in the emission region, which is dominated by reprocessed photons from an accretion disc, if present. The relation with luminosity/power could be indirect, due to the fact that a bright accretion disc forms only for high values of the accretion rate in Eddington units (e.g. $\dot{m} > 10^{-2}\dot{m}_{\text{crit}}$), while the absence of it (RIAF, radiatively inefficient accretion flows) occurs for $\dot{m} < 10^{-2}\dot{m}_{\text{crit}}$, thus at lower power for a fixed mass of the accreting black hole. Thus, the original picture of blazar SEDs, as a one-parameter family governed by luminosity, should be revised including the mass of the accreting black hole as an additional important parameter. A new scheme along these lines has been recently suggested by Ghisellini & Tavecchio (2008).

ACKNOWLEDGMENTS

We thank an anonymous referee for useful comments. This research has made use of data obtained from the High Energy Astrophysics Science Archive Research Center (HEASARC), provided by NASA’s Goddard Space Flight Center.

This research has made use of the NED which is operated by the Jet Propulsion Laboratory, California Institute of Technology, under contract with the National Aeronautics and Space Administration.

Funding for the SDSS and SDSS-II has been provided by the Alfred P. Sloan Foundation, the Participating Institutions, the National Science Foundation, the US Department of Energy, the National Aeronautics and Space Administration, the Japanese Monbukagakusho, the Max Planck Society and the Higher Education Funding Council for England. The SDSS web site is <http://www.sdss.org/>. The SDSS is managed by the Astrophysical Research Consortium for the Participating Institutions. The Participating Institutions are the American Museum of Natural History, Astrophysical Institute Potsdam, University of Basel, University of Cambridge, Case Western Reserve University, University of Chicago, Drexel University, Fermilab, the Institute for Advanced Study, the Japan Participation Group, Johns Hopkins University, the Joint Institute for Nuclear Astrophysics, the Kavli Institute for Particle Astrophysics and Cosmology, the Korean Scientist Group, the Chinese Academy of Sciences (LAMOST), Los Alamos National Laboratory, the Max-Planck-Institute for Astronomy (MPIA), the Max-Planck-Institute for Astrophysics (MPA), New Mexico State University, Ohio State University, University of Pittsburgh, University of Portsmouth, Princeton University, the United States Naval Observatory and the University of Washington.

We acknowledge funding from ASI/INAF with contract I/088/06/0.

REFERENCES

- Aharonian F. et al., 2008, *A&A*, 481, L103
 Barthelmy S. D. et al., 2005, *Space Sci. Rev.*, 120, 143
 Bassani L. et al., 2007, *ApJ*, 669, L1
 Bassett L. C., Brandt W. N., Schneider D. P., Vignali C., Chartas G., Garmire G. P., 2004, *AJ*, 128, 523
 Burrows D. N. et al., 2005, *Space Sci. Rev.* 120, 165
 Caccianiga A., Marchā M. J. M., 2004, *MNRAS*, 348, 937
 Cappi M., Matsuoka M., Comastri A., Brinkmann W., Elvis M., Palumbo G. G. C., Vignali C., 1997, *ApJ*, 478, 492
 Cardelli J. A., Clayton G. C., Mathis J. S., 1989, *ApJ*, 345, 245
 Celotti A., Ghisellini G., 2008, *MNRAS*, 385, 283 (CG08)
 Costamante L., Ghisellini G., 2002, *A&A*, 384, 56
 Decarli R., Dotti M., Fontana M., Haardt F., 2008, *MNRAS*, 386, L15
 Fabian A. C., Celotti A., Iwasawa K., McMahon R. G., Carilli C. L., Brandt W. N., Ghisellini G., Hook I. M., 2001a, *MNRAS*, 323, 373
 Fabian A. C., Celotti A., Iwasawa K., Ghisellini G., 2001b, *MNRAS*, 324, 628
 Falco E. E., Kochanek C. S., Munoz J. A., 1998, *ApJ*, 494, 47
 Finke J. D., Dermer C. D., Böttcher M., 2008, *ApJ*, 686, 181
 Fiore F., Elvis M., Giommi P., Padovani P., 1998, *ApJ*, 492, 79
 Foschini L., et al., 2007, *ApJ*, 657, L81
 Foschini L. et al., 2008, *A&A*, 484, 35
 Fossati G., Maraschi L., Celotti A., Comastri A., Ghisellini G., 1998, *MNRAS*, 299, 433
 Gehrels N. et al., 2004, *ApJ*, 611, 1005
 Georganopoulos M., Kazanas D., 2003, *ApJ*, 594, L27
 Ghisellini G., Tavecchio F., 2008, *MNRAS*, 387, 1669
 Ghisellini G., Celotti A., Fossati G., Maraschi L., Comastri A., 1998, *MNRAS*, 301, 451
 Ghisellini G., Celotti A., Costamante L., 2002, *A&A*, 386, 833
 Ghisellini G., Tavecchio F., Chiaberge M., 2005, *A&A*, 432, 401
 Gioia I. M., Maccacaro T., Schild R. E., Wolter A., Stocke J. T., Morris S. L., Henry J. P., 1990, *ApJS*, 72, 567
 Giommi P., 2008, *Mem. Soc. Astron. Ital.*, 79, 154
 Giommi P. et al., 2007a, *A&A*, 468, 571
 Giommi P. et al., 2007b, *A&A*, 468, 97
 Goldwurm A. et al., 2003, *A&A*, 411, L223
 Grandi P., Malaguti G., Fionocchi M., 2006, *ApJ*, 642, 113
 Guainazzi M. et al., 2006, *A&A*, 446, 87
 Healey S. E. et al., 2008, *ApJS*, 175, 97
 Kalberla P. M. W. et al., 2005, *A&A*, 440, 775
 Kaspi S., Brandt W. N., Maoz D., Netzer H., Schneider D. P., Shemmer O., 2007, *ApJ*, 659, 997
 Komossa S. et al., 2006, *ApJ*, 132, 531
 Konopelko A., Mastichiadis A., Kirk J., de Jager O. C., Stecker F. W., 2003, *ApJ*, 597, 851
 Krawczynski H., Coppi P. S., Aharonian F., 2002, *MNRAS*, 336, 721
 Lähteenmäki A., Valtaoja E., 1999, *ApJ*, 521, 493
 Lähteenmäki A., Valtaoja E., Wiik K., 1999, *ApJ*, 511, 112
 Landt H., Perlman E., Padovani P., 2006, *ApJ*, 637, 183
 Landt H., Padovani P., Giommi P., Perri M., Cheung C. C., 2008, *ApJ*, 676, 87
 Laurent-Muehleisen S. A. et al., 1999, *ApJ*, 525, 127
 Lebrun F. et al., 2003, *A&A*, 411, L141
 Ledden J. E., O'Dell S. L., 1985, *ApJ*, 298, 630
 Malizia A. et al., 2008, *MNRAS*, 389, 1360
 Maraschi L., Tavecchio F., 2001, in Padovani P., Urry C. M., eds, *ASP Conf. Ser. Vol. 227, Blazar Demographics and Physics*. Astron. Soc. Pac., San Francisco, p. 40
 Maraschi L., Tavecchio F., 2003, *ApJ*, 593, 667
 Maraschi L., Ghisellini G., Tavecchio F., Foschini L., Sambruna R. M., 2008, preprint (arXiv:0802.1789)
 Marconi A., Axon D. J., Maiolino R., Nagao T., Pastorini G., Pietrini P., Robinson A., Torricelli G., 2008, *ApJ*, 678, 693
 Massaro E., Sclavi S., Giommi P., Perri M., Piranomonte S., 2005, *Multi-frequency Catalogue of Blazars*, Vol. 1. Aracne Editrice, Roma
 Massaro E. et al., 2008, *Multifrequency Catalogue of Blazars*, Vol. 2. Aracne Editrice, Roma
 Nieppola E., Tornikoski M., Valtaoja E., 2006, *A&A*, 445, 441
 Nieppola E., Valtaoja E., Tornikoski M., Hovatta T., Kotiranta M., 2008, *A&A*, 488, 867
 Padovani P., 2007, *Ap&SS*, 309, 63
 Padovani P., Costamante L., Ghisellini G., Giommi P., Perlman E., 2002, *ApJ*, 581, 895
 Pian E., Treves A., 1993, *ApJ*, 416, 130
 Piner B. G., Pant N., Edwards P. G., 2008, *ApJ*, 678, 64
 Roming P. W. A. et al., 2005, *Space Sci. Rev.*, 120, 95
 Sambruna R. M. et al., 2006a, *ApJ*, 646, 23
 Sambruna R. M., Gliozzi M., Tavecchio F., Maraschi L., Foschini L., 2006b, *ApJ*, 652, 146
 Sikora M., 2001, in Padovani P., Urry C. M., eds, *ASP Conf. Ser. Vol. 227, Blazar Demographics and Physics*. Astron. Soc. Pac., San Francisco, p. 95
 Sikora M., Begelman M. C., Rees M. J., 1994, *ApJ*, 421, 153
 Stocke J. T., Morris S. L., Gioia I. M., Maccacaro T., Schild R., Wolter A., Fleming T. A., Henry J. P., 1991, *ApJS*, 76, 813
 Tagliaferri G. et al., 2008, *ApJ*, 679, 1029
 Tavecchio F., 2007, *Ap&SS*, 311, 247
 Tavecchio F. et al., 2000, *ApJ*, 543, 535
 Tavecchio F., Maraschi L., Ghisellini G., Kataoka J., Foschini L., Sambruna R. M., Tagliaferri G., 2007, *ApJ*, 665, 980
 Toor A., Seward F. D., 1974, *AJ*, 79, 995
 Turriziani S., Cavazzuti E., Giommi P., 2007, *A&A*, 472, 699
 Valtaoja E., Lähteenmäki A., Teräsanta H., Lainela M., 1999, *ApJS*, 120, 95
 Vignali C., Brandt W. N., Schneider D. P., 2003, *AJ*, 125, 433
 Wagner R. M., 2008, *MNRAS*, 385, 119
 Wolter A., Celotti A., 2001, *A&A*, 371, 527
 Yuan W., Zhou H. Y., Komossa S., Dong X. B., Wang T. G., Lu H. L., Bai J. M., 2008, *ApJ*, 685, 801

This paper has been typeset from a \LaTeX file prepared by the author.